Nanoscale Advances

ROYAL SOCIETY OF CHEMISTRY

PAPER

View Article Online
View Journal | View Issue

Cite this: *Nanoscale Adv.*, 2024, **6**, 1704

Influence of arylalkyl amines on the formation of hybrid $CsPbBr_3$ nanocrystals *via* a modified LARP method†

Ernest Ruby,[a] Hugo Levy-Falk,[a] Gaëlle Trippé-Allard,[a] Frédéric Fossard,[b] Maxime Vallet,[cd] Nicolas Guiblin,[c] Jean-Sébastien Lauret,[a] Emmanuelle Deleporte[a] and Cédric R. Mayer *[a]

Perovskite nanocrystals have attracted much attention in the last ten years due to their different applications, especially in the photovoltaic domain and LED performance. In this large family of perovskite nanocrystals, $CsPbBr_3$ nanocrystals are attractive nanomaterials because they are good candidates for obtaining green emissions and exploring new synthesis routes. In this context, controlling the nanometric scale's morphology, particularly the size and monodispersity, is fundamental for exploring their photophysical properties and final applications. Currently, the nanometric size of nanocrystals is ensured by the presence of oleic acid and oleylamine molecules, in using Hot Injection (HI) or ligand-assisted reprecipitation (LARP) methods. If oleic acid plays a fundamental role, oleylamine can be easily substituted by other amino molecules, opening the way for the functionalization of $CsPbBr_3$ nanocrystals and the obtention of new hybrid perovskite nanocrystal families. In this article, we describe the synthesis, by soft chemistry, of a new family of hybrid organic–inorganic $CsPbBr_3$ nanocrystals, functionalized by aryl-alkylamine (AAA) molecules, through the modified LARP method. We highlight the mechanism for cutting submicron crystals into nanocrystals, using aryl-alkylamine molecules like scissors. The impact of these amino molecules on the final nanocrystals leads to different nanocrystal morphologies (nanocubes, nanosheets, or nanorods) and structures (monoclinic, rhombohedral, or tetragonal). In addition, this modified LARP method highlights, under certain experimental conditions, an unexpected formation of PbO ribbons.

Received 12th December 2023
Accepted 28th January 2024

DOI: 10.1039/d3na01105d

rsc.li/nanoscale-advances

1 Introduction

Modern electronic devices, such as TVs, smartphones, and automotive screens, are increasingly oriented towards flexible supports, but inorganic semiconductors have reached a technological deadlock. Printed electronics appear to be a real alternative to solve this problem.[1] A new class of nanoscale semiconductors, $CsPbBr_3$ nanocrystals, has seen a real surge in interest because it addresses the emerging demands in optoelectronic devices, like flexible displays and organic photovoltaic systems. They can offer flexibility comparable to their all-organic counterparts while delivering performance on par with traditional inorganic semiconductors.[2–4] $CsPbBr_3$ is the most famous perovskite material,[5] particularly studied under a nanometric scale for its optoelectronic properties.[6–9] Nevertheless, the performance of an optimal optoelectronic flexible device requires the highest degree of uniformity in terms of nanocrystal size and shape in large-scale volumes. This homogeneous distribution is crucial to facilitate the self-assembly of these cubic nanocrystals within the active layer of optoelectronic devices. Another crucial point in a technological transfer concerns the synthesis conditions to produce these nanocrystals in large-scale volumes.

Many teams are devoted to the synthesis of perovskite nanocrystals in different media or with different morphologies. Jasieniak and colleagues have reported the synthetic evolution of this class of semiconductors.[10] Among these descriptions, the Hot Injection (HI) method described by Kovalenko's team, using oleic acid (OA), oleylamine (OAm), energetic conditions (with very high temperatures (140–200 °C)), and an inert atmosphere, leads to high monodispersity of $CsPbBr_3$

[a]*Université Paris-Saclay, ENS Paris-Saclay, CentraleSupélec, CNRS, LuMIn (UMR 9024), Gif-sur-Yvette, France. E-mail: cedric.mayer@ens-paris-saclay.fr*
[b]*Université Paris-Saclay, ONERA, CNRS, Laboratoire d'étude des Microstructures, 92322, Châtillon, France*
[c]*Université Paris-Saclay, CentraleSupélec, CNRS, Laboratoire SPMS (UMR8580), 91190, Gif-sur-Yvette, France*
[d]*Université Paris-Saclay, ENS Paris-Saclay, CentraleSupélec, CNRS, LMPS – Laboratoire de Mécanique Paris-Saclay (UMR 9026), 91190, Gif-sur-Yvette, France*

† Electronic supplementary information (ESI) available: Synthesis and characterization details; PL lifetime-decay curves, UV-vis light irradiation, time-resolved photoluminescence (TRPL) decay curve, XRD patterns, and TEM image; size distribution histogram of AAA-$CsPbBr_3$ nanocrystals. See DOI: https://doi.org/10.1039/d3na01105d

nanocrystals in size and shape.[11–13] Even though the HI method leads to highly calibrated nanocrystals, this method could limit a technological transfer for industrial production due to these specific conditions. An alternative way is a ligand-assisted precipitation (LARP) method. This method operates in an ambient atmosphere at room temperature.[14] It consists of the precipitation of cation reagents Pb^{2+} and Cs^{+} (solubilized in a polar solvent) in an apolar solvent, leading to perovskite nanocrystals, with the help of OA and OAm, like the HI method. However, this method leads to nanocrystals with wide distributions in size and shape.[15] Whatever the methods, several parameters impact the quality of the final nanocrystal solutions and their properties: the nature and molarity of amines,[16,17] the ratio of Cs^{+} in regard to Pb^{2+} cations,[18] the ratio of oleic acid,[19–22] and the nature of polar and apolar solvents.[23] Otherwise, whatever the type of inorganic nano-particles their organic functionalization is also an important point to stabilize them or to add complementary properties.[24] Perovskite materials are no exception to the rule, with the use of different long-chain alkylamines,[25] alkylammoniums,[26,27] or alkyl or aryl carboxylic acids.[28] However, with both previously cited methods (HI and LARP methods), the simple modification of one reagent can affect drastically the final nanocrystals (like the size, shape, or stability).[29–31]

Recently, our team reported a facile and original way to synthesize monodisperse $CsPbBr_3$ nanocrystals in large proportion based on the modified-LARP (MLARP) method, using phenylethylamine (PEA) molecules.[32] Our method showed that PEA acted as scissors to cut big $CsPbBr_3$ nanocrystals into smaller high-calibrated nanocrystals. PEA is commonly used as a second amine with OAm to functionalize nanocrystals,[33–35] for synthesizing 2D–3D perovskite film, and for solar cells and light-emitting devices.[36–39] We highlighted the fundamental role of amino groups in this method. We demonstrated that PEA was the reagent responsible for cutting preformed particles into highly calibrated nanocrystals. In this protocol, similar optical properties of the nanocrystals in solution or drop-cast films on quartz substrates have been observed and it has been suggested that some homogeneous thin films of these nanoparticles could be made, without degrading the optical performances of the nanocrystals while keeping them stable.

MLARP opens a new way toward a large panel of hybrid organic–inorganic perovskite $CsPbBr_3$ nanocrystals. So, since phenylethylamine (PEA) has proved to be a promising molecule for MLARP, other molecules of this family, such as aryl alkylamines (so-called AAA), have to be tested to generalize this new method. The AAA molecules open the way to the functionalization of perovskite nanocrystals and to organic conjugated molecules with optical or electronic properties.

This work extends the modified-LARP method (MLARP) to a large panel of aryl alkyl-amine (AAA) molecules with a general formula of R–Ph–R′–NH_2. The main aim of this study is to understand the effect of the nature of AAA on the formation of $CsPbBr_3$ nanocrystals. In this context, we highlight the influence of the length of the alkyl chain through R′, the steric hindrance of R, and the use of amino acids on the final nature of nanocrystals (form, size, and polydispersity). For a large part of them, this method allows reaching very high monodisperse nanocrystals under soft chemistry conditions, without the need for several centrifugation steps and high temperature. We show that the chemical structure of AAA molecules has a real impact on the morphology, stability, calibration, and performance of photoluminescence quantum yields (PLQYs) of these functionalized $CsPbBr_3$ nanocrystals.

2 Results and discussion

As stated in the introduction section, $CsPbBr_3$ nanocrystals are highly promising semiconductors in the field of organic electronics, particularly in the field of printed electronics. Therefore, they are intended to be associated with organic matrices that are also semiconductors. Thus, the functionalization of NCs with AAA is crucial for a potential good interaction between the nanocrystal and its organic matrix. However, the use of direct arylamines (such as aniline and its derivatives) leads to the complete degradation of the initial $CsPbBr_3$ nanocrystals. Therefore, the addition of an alkyl group is necessary. On the other hand, it was interesting to evaluate the impact of chain length on the formation of nanocrystals. Regarding the aromatic part, we are interested in evaluating the influence of electron-donating groups, polyaromatic systems, and groups exhibiting steric hindrance, to fully investigate a large panel of AAA. We have shared this study in four series to cover a large panel of AAA (R–Ph–R′–NH_2). We have focused our attention on three alkyl linkers (methylene –CH_2–, ethylene –C_2H_4– and propylene –C_3H_6– groups), with different R–Ph groups (particularly with methylene and ethylene linkers). We have also studied two amino acids, $AmAc_1$ and $AmAc_2$, to control the

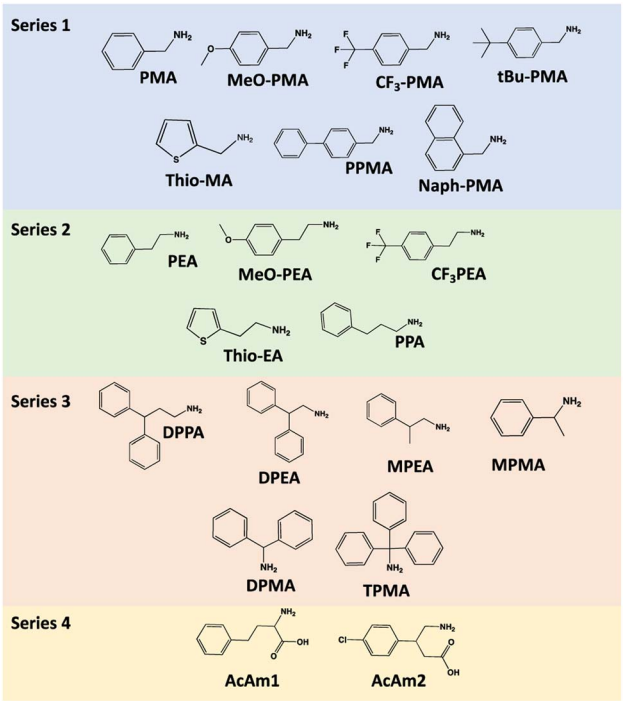

Scheme 1 Summary of the AAA molecules studied in this work.

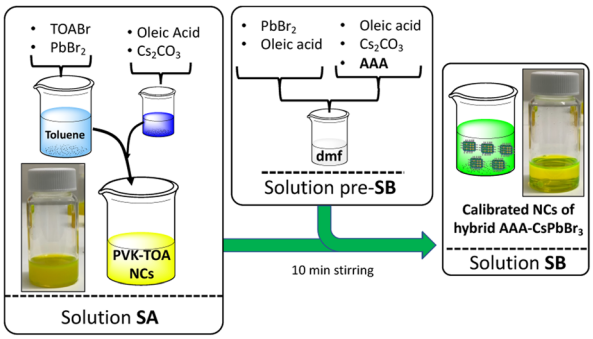

Scheme 2 Schematic representation of the synthesis of these high-calibrated nanocrystals.

influence of the carboxylate group close to the amine function (Scheme 1) because this organic function can also functionalize perovskite surfaces. Series 1 is dedicated to methylene linkers, series 2 to ethylene and propylene linkers, series 3 to molecules with steric hindrance, and the last series to two amino acids (Scheme 1).

The synthesis method is similar to our previous work.[32] However, the ratio of AAA/Pb^{2+} has been optimized following the nature of AAA to get better stability and calibration of the functionalized nanocrystals. This ratio ranges between 0.4 and 1 (see Table SI-1†). To recall this process, the synthesis method is illustrated in Scheme 2.

Afterward, to clarify the text, as all perovskites are based on $CsPbBr_3$, we will call the $CsPbBr_3$ nanocrystals obtained after cutting by AAA, AAA-NCs. So, AAA-NCs will stand for $CsPbBr_3$ nanocrystals functionalized by the AAA molecule (Scheme 2).

2.1 Evidence of the functionalization of nanocrystals by AAA

The aim of this study is to highlight the functionalization of perovskite nanocrystals by organic molecules. To do this, we used two markers, one containing a $-CF_3$ group to detect the presence of fluorine atoms, and the second one, a baclofen molecule, which contains a chlorine atom. CF_3–PEA has been used to check the presence of AAA on the nanocrystal surface and the functionalization of nanocrystals by the AAA molecules. By EDS in HAADF-STEM, fluoride atoms (Fig. 1d) are detected with a similar level and at the same place as nanocrystals (Fig. 1b) or other elements, Pb (Fig. 1c), Cs (Fig. 1f) and Br (Fig. 1e) atoms, confirming the passivation of nanocrystals by AAA (Fig. 1).

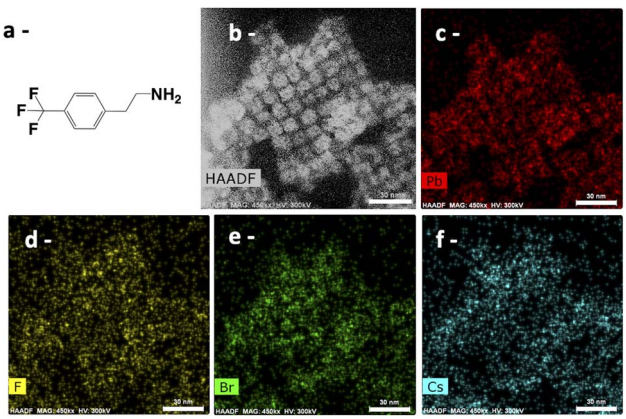

Fig. 1 HAADF-STEM analysis of CF_3PEA-NCs (scale bar: 30 nm): (a) scheme of the molecule; (b) in HAADF and by EDS to visualize (c) Pb element; (d) F element; (e) Br element; and (f) Cs element.

A similar result has been obtained with baclofen, $AmAc_2$-NCs: EDS analysis (Fig. SI-40†) highlights the presence of chlorine atoms on the surface of nanocrystals, in parallel with the detection of lead, cesium, and bromine atoms (Fig. SI-40†), indicating the presence of $AmAc_2$ on the nanocrystal surface.

2.2 Influence of AAA molecules on the nature, morphology, and ordering of nanocrystals

The influence of AAA molecules on the nature and morphology of nanocrystals has been analyzed with the same protocol. For each series of samples, the AAA-NCs were analyzed by optical spectroscopy and in addition, we simultaneously prepared a film on a glass substrate and a TEM grid. The films are obtained by drying a drop of solution (~200 μL) at room temperature and are used for X-ray diffraction characterization. The TEM grids are prepared by dropping a small amount of solution (~1 μL) on the copper grid and then sucking the solvent with absorbent paper. This process limits the concentration of nanocrystals on the copper grid. All samples were compared with the PVK-TOA nanocrystals (starting with the larger $CsPbBr_3$ nanocrystals) used to prepare them, for reference purposes. Using this protocol, a correspondence can be applied between the optical spectroscopy, TEM, and XRD analysis for each sample.

2.2.1 First series with a methylene R′ ($-CH_2-$) linker. At first, we analyzed a first group of seven AAA organic molecules (PMA, MeO–PMA, *t*Bu–PMA, CF_3–PMA, Thio–MA, PPMA, and Naph–PMA), with only one methylene group between the amino group and the aryl part. They have been selected for their different functional groups (donor groups like MeO-Ph, *t*Bu-Ph, thiophene, or electron-attracting groups such as CF_3–) and polyaromatic configurations (phenyl–aryl- or naphthalene moieties).

The sizes of the corresponding nanocrystals have been analyzed by TEM on more than 2000 nanocrystals (up to 3900) for each one, yielding an average size of approximately 10.3 nm ± 3.7 nm (Table 1) for PMA-NCs, *t*BuPMA-NCs, MeOPMA-NCs, and CF_3PMA-NCs and a narrow size distribution of nanocrystals around 12 nm ± 3.4 nm for NaphPMA-NCs, PPMA-NCs, and ThioMA-NCs as shown in Table 1 (Table SI-3†). For PMA-NCs, *t*BuPMA-NCs, and MeOPMA-NCs solutions, their stability remains for over two weeks (without flocculation or aggregation of nanocrystals). For ThioMA-NCs, PPMA-NCs, NaphPMA-NCs, and CF_3PMA-NCs, the solutions become orange in a few days (Table 1) and a precipitate is observed. This difference in stability is certainly due to the formation of nanocrystal aggregates as those observed by TEM.

TEM analyses also highlight with PMA-NCs (Fig. 2a), *t*BuPMA-NCs (Fig. 2b), and MeOPMA-NCs (Fig. 2c) some

Table 1 Summary of different characteristics of AAA-NCs

Samples-NCs	λ^a (em)	FWMH (nm)	QY	$\tau_{(ampl)}$	Stability[b]	Shape[c]	Average size (nm)
PVK TOA	517	18	11%	11.05	+	PD	38
PMA	516.5	18	64%	17.25	+++	NCs	11.83
MeO–PMA	516.5	18	78%	18.15	+++	NCs	9.91
TBu–PMA	516	18	81%	18.52	+++	NCs	12.4
CF_3–PMA	516	18	56%	22.3	+	NCs	9.4
Thio–MA	515	18	42%	12.64	+	NCs	13.2
4-PPMA	517	18	59%	14.53	++	NCs	9.74
Naph–PMA	518	18	62%	17.4	++	NCs	11
PEA	516	18	61%	13.96	+++	NCs	10.1
CF_3–PEA	516.5	18	70%	12.94	++	NCs	13.7
MeO–PEA	516	18	70%	16.55	+++	NCs	9.87
Thio–EA	516	18	55%	17.32	+	NCs	nd[d]
PPA	516	18	80%	14.5	+++	NCs	8.14
MPMA	521	>19	41%	17.53	+	NCs	14.02
MPEA	516	18	64%	16.91	++	NCs	11.04
DPEA	518	18	45%	22.36	+	NRs	17.4
DPPA	515	18	71%	17.4	++	NCs	11.9
TPMA	522	>19	5%	nd	—	nd	nd
DPMA	521	>19	8%	nd	—	nd	nd
AA2	519	>19	40%	24.89	—	PD	11.7
AA1	520	>19	19%	37.8	—	NWs	nd

[a] Measured after the synthesis. [b] +++: very stable for several weeks, ++: stable for one week, +: stable for 1–2 days, —: unstable. [c] NCs: nanocubes, NRs: nanorods, NWs: nanowires, PD: polydisperse. [d] nd: undetermined.

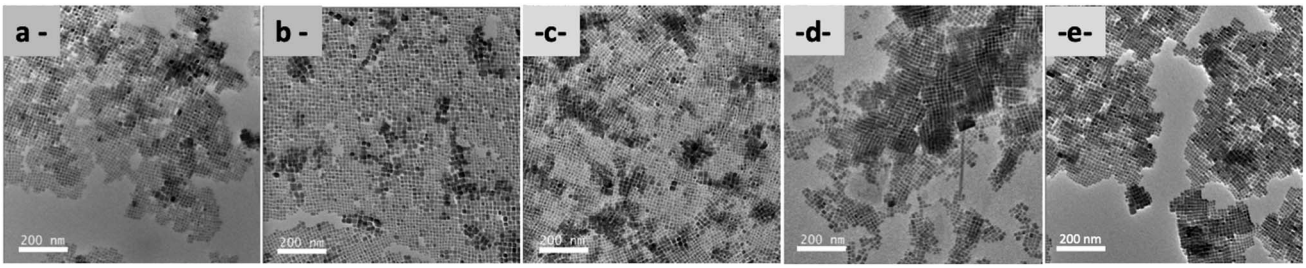

Fig. 2 TEM (200 kV) images (scale bar: 200 nm) of (a) PMA-NCs; (b) *t*BuPMA-NCs; (c) MeOPMA-NCs; (d) NaphPMA-NCs; and (e) ThioMA-NCs.

crystals' ordered arrangement in a 2D superlattice on the copper grid.

With NaphPMA-NCs (Fig. 2d), PPMA-NCs (Fig. SI-7†), and ThioMA-NCs (Fig. 2e), some 3D-assemblies, like super-crystal structures (Scheme 3), are observed on the copper grid.[40–42]

This ordering leads to the formation of columns of highly calibrated nanocrystals, like a stack of Lego® bricks (Scheme 3).

With CF_3PMA-NCs and with a diluted drop, linear arrangements of nanocrystals are observed (Fig. 3). The other AAA-NCs do not show this type of linear arrangement under similar conditions of observation and drop dilution.

This series, based on methylene as a linker, shows that the MLARP synthesis is efficient in obtaining highly calibrated nanocrystals with an apparent cubic form. The impact of the functional group of the molecule plays a role in the stability of the solution. When the functional group is a heterocycle like a thiophene or an extended aromatic group like the 4-phenylbenzylamine (PPMA) or the naphthalene group, these groups promote aggregation of NCs certainly due to the nature of the aromatic group leading to some kinds of π-stacking interactions between nanocrystals and also the size of NCs being slightly larger.

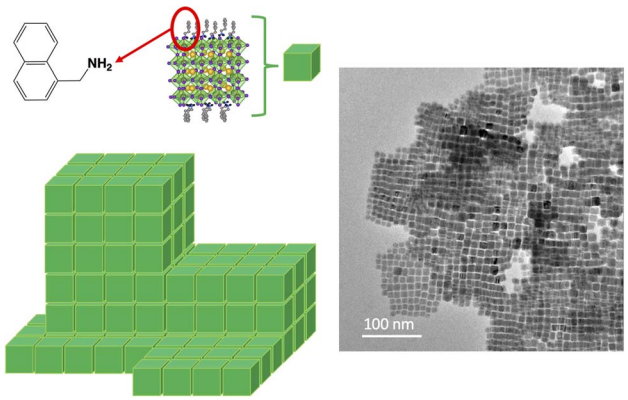

Scheme 3 Schematic representation of the starting 3D-superlattice of Naph–PMA nanocrystals and the corresponding TEM pictures.

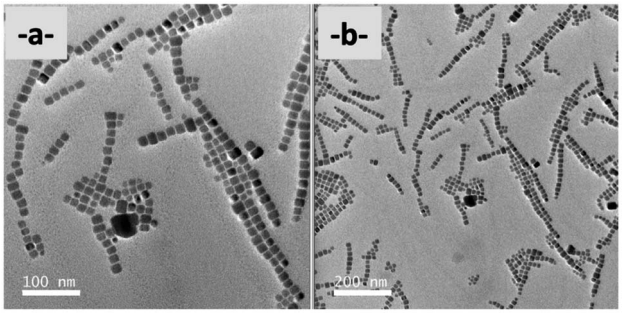

Fig. 3 TEM images (200 kV) of CF_3–PMA nanocrystals, (a) scale bar 100 nm and (b) scale bar 200 nm.

Concerning XRD analysis and optical studies, all samples have been analyzed under the same conditions, at the same delay after synthesis, and from the same initial PVK-TOA nanocrystals. About XRD analysis, the LARP method generally generates nanocrystals with a monoclinic structure,[43–45] as is the case for our starting PVK-TOA nanocrystals (from SA solution), analyzed previously.[32] Several AAA-nanocrystals, drop-cast films onto a glass slide, present XRD patterns indexed to the monoclinic structure, with the same indexation lines ((010), (100), (110), (020) and (200), reference PDF#18-0364), *t*BuPMA-NCs (Fig. 4a), MeOPMA-NCs (Fig. 4b), and PhPMA-NCs (Fig. 4c). So, these patterns look similar to PVK structures obtained by J. J. Jasieniak *et al.* with PVKs so-called TOL-LARP (toluene-LARP) or EA-LARP (ethyl acetate-LARP).[43,44] But, in the literature, other synthesis methods of $CsPbBr_3$ nanocrystal structures can also be indexed to an orthorhombic structure.[13,46,47] Nevertheless, it can be difficult to distinguish both structures due to the close indexation of different peaks, particularly when the lines are not well-defined. Thus, for CF_3PMA-NCs, the pattern is closer to an orthorhombic structure, with the same indexation lines ((002), (110), (004), and (220), reference PDF#97851). This conversion of structure, from monoclinic to orthorhombic, is certainly due to the action of these AAA molecules on the nanocrystal surface, which induces some crystallographic constraints and structural modifications.[48] We can observe for PMA-NCs and MeOPMA-NCs that there are two small additional lines at 12.72° and 25.54° ((102) and (204) planes respectively), due to the presence of Cs_4PbBr_6 structures on glass plates (PDF#73-2478).[45,49–53] This structure has not been observed during the TEM analysis. This secondary structure appears during the sample XRD preparation and more particularly during the evaporation of the solvent, which induced a transformation of the $CsPbBr_3$ nanocrystal (detailed in Section 2.4).

Concerning optical studies, all the nanocrystals exhibit green emission peaks centered around 516 nm ($E_{max}^{PL} = 2.41$ eV, Fig. SI-3†) with a narrow full width at half maximum (FWHM <18 nm). This result reflects the good monodispersity of the nanocrystals. Another impact of organic molecules on nanocrystals is their PL quantum yield (PLQY, Tables SI-2† and 1). For this series, we obtained a very high PLQY of around 80% for *t*BuPMA-NCs, 78% for MeOPMA-NCs, and for the others around 60%, except for ThioMA-NCs (only 45%). This lower value aligns with the limited stability of the solution, suggesting the presence of aggregates already present in the solution.

2.2.2 Second series with ethylene (–C_2H_4–) and propylene (–C_3H_6–) linkers. Secondly, we extended the linker between the amino group and aryl group, with an ethyl or propyl group linker. In this new series, we tested CF_3–PEA (Fig. 1g and SI-20†), MeO–PEA (Fig. SI-22), Thio–EA (Fig. SI-24), and PPA (Fig. SI-25†) molecules. PEA was studied in our previous work.[32]

Regarding the calibration of nanocrystals, CF_3PEA-NCs (Fig. SI-20†) and MeOPEA-NCs are highly calibrated with a narrow size of 11 nm ± 2.6 nm and stable (unaggregated) over 7 days (Fig. SI-23†). ThioEA-NCs (Fig. 5) have a particular behavior. ThioEA-NCs are also well calibrated but these nanocrystals appear by TEM, on a copper grid, like an aggregated porous network and the solution becomes orange after a few hours, to finally fully precipitate after a couple of days. In this

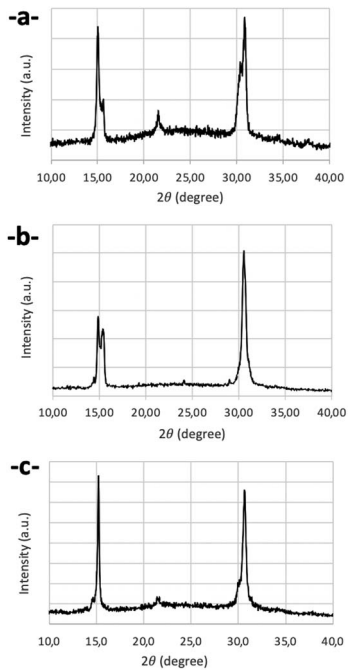

Fig. 4 XRD patterns of (a) *t*BuPMA-NCs, (b) MeOPMA-NCs, and (c) PhPMA-NCs.

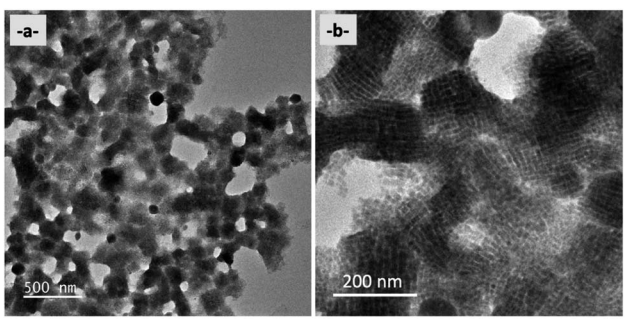

Fig. 5 TEM (200 kV) pictures of Thio–EA nanocrystals with scale bar (a) 500 nm and (b) 200 nm.

particular case, the linker between the thiophene moiety and the amino group plays a role in the state of nanocrystal assemblies on a copper grid. The $-CH_2-$ (methylene linker group between aryl part and $-NH_2$ function) group forces the aromatic part to be almost parallel to the nanocrystal surface, leading to some well 3D assembly. On the other hand, with an ethylenic group, the ethylene part gives more flexibility to aromatic moieties, and the groups can be more disordered on the surface and induce a disorder in the assembly, leading to a porous network.

In addition, PPA has been tested to study the influence of complementary $-CH_2-$ compared to the ethylene group. TEM analysis shows a good calibration of nanocrystals with a smaller size distribution centered at 8 nm ± 4.1 nm (on 1553 nanocrystals) (Fig. SI-26†). The solution of PPA-NCs is very stable for several weeks.

XRD analysis, like with the first series, depending on the AAA molecules, shows monoclinic (PEA and PPA) and orthorhombic structures (MeOPEA-NCs, ThioEA-NCs, and CF_3PEA-NCs).

In photoluminescence, when the solutions are observed just after the synthesis, the nanocrystals exhibit green emission peaks centered around 516 nm ($E_{max}^{PL} = 2.41$ eV, Fig. SI-5†) with narrow full width at half maximum (FWHM ≈18 nm), even for ThioEA-NCs. For this last one, this result shows that nanocrystals are well-calibrated. However, for ThioEA-NCs, the emission decreases after a few hours with the aggregation of NCs in the solution.

About PLQY, the minor modifications to the synthesis compared with our previous work have allowed us to achieve better stability and calibration of nanocrystals, and consequently a higher PLQY, with PEA-NCs (61%) and a great value with PPA-NCs (80%). For MeOPEA-NCs and CF_3PEA-NCs, the same PLQY value is obtained (70%). Similar to ThioMA-NCs, ThioEA-NCs also exhibit a lower value, at 55%, certainly due to the presence of smaller aggregates in the solution (Tables 1 and SI-2†).

2.2.3 Third series with the hindrance effects. We operated a new series of amino molecules with hindrance effects on AAAs, with DPPA, DPEA, MPEA, MPMA, DPMA, and TPMA molecules.

For DPPA-NCs, DPEA-NCs, MPEA-NCs, and MPMA-NCs, the solutions are stable for only a couple of days. The solutions became yellow-orange to orange and precipitated after seven days. However interesting results appear concerning the shape of the nanocrystals. A noticeable difference between the first four MPMA, MPEA, DPEA, and DPPA nanocrystals can be observed in TEM. MPEA (Fig. SI-28†) and DPPA (Fig. SI-34†) are very highly calibrated nanocrystals, but smaller with MPEA (8.9 nm ± 3.8 nm over 1559 particles, Fig. SI-29†) compared to DPPA (11.9 nm ± 3.5 nm over 2000 particles, Fig. SI-35).† With the MPMA molecule (Fig. SI-37),† the nanocrystals tend towards a higher calibration but the cutting process is not completed. The most surprising result concerns nanocrystals based on DPEA that exhibit two types of nanostructures coexisting in the solution: long rods, having a size of around 200 nm by 10 nm, stacked following their lengths (Fig. 6a) (both in Fig. SI-31†) presenting a certain polydispersity in length, and small nanorods, of size 20 × 10 nm, that are well-calibrated (Fig. 6b). The growing axe direction is along the (100) superlattice for both types of nanorods.[54–56]

The nanorods are linked together on the side corresponding to the (010) plane. We observe also long rods, particularly along the (010) planes. However, they are not well-calibrated in form, with unregular growth (Fig. 7c). Using HAADF-STEM these nanorods are assembled like bunches of grapes (Fig. 8c). It's the same for long nanorods, linked together following their length by undefined structures (Fig. SI-31c and d†). So, the action of DPEA molecules leads to unexpected results in the final structures and highlights the role of organic molecules during this MLARP process.[57–59] This particularity is certainly due to the

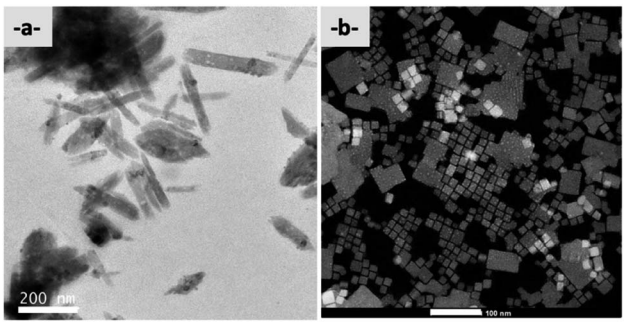

Fig. 7 (a) TEM (200 kV) pictures of $AcAm_1$ (scale bar 200 nm) and (b) HRSTEM in HAADF of $AcAm_2$ nanocrystals (scale bar 100 nm).

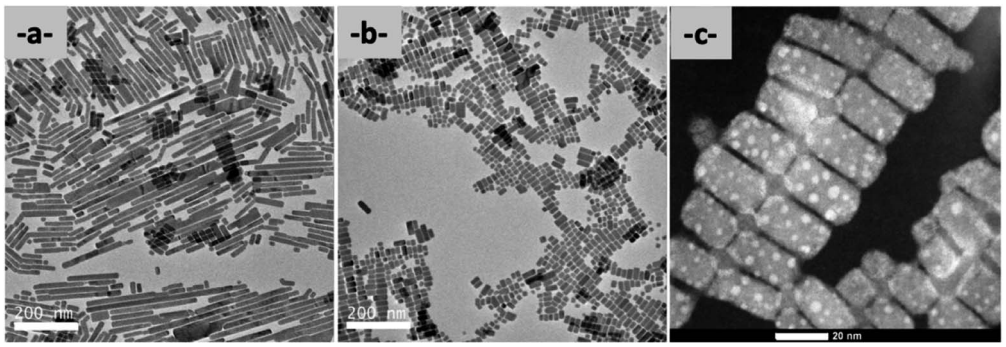

Fig. 6 TEM analysis of DPEA-NCs (a) by TEM (200 kV, scale bar 200 nm) of long rods; (b) by TEM (200 kV, scale bar 200 nm) of small rods, and (c) by HAADF-STEM of these small rods (scale bar 20 nm).

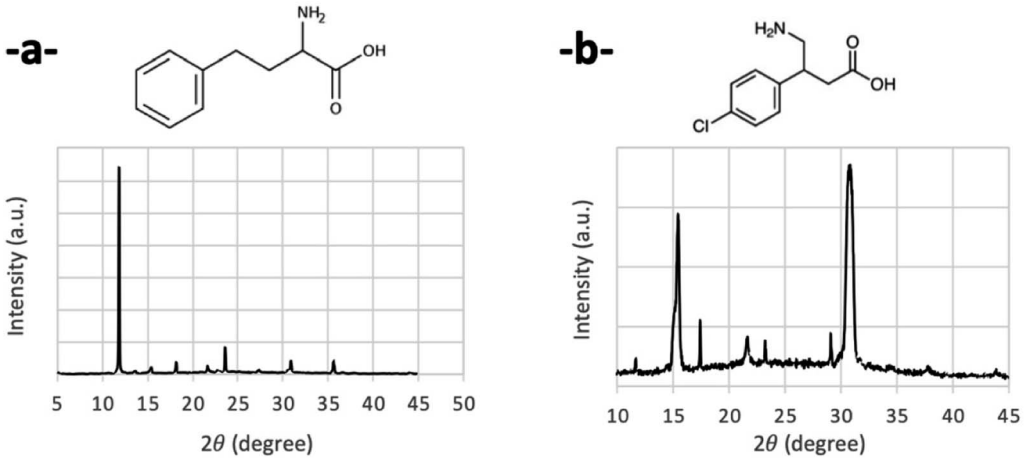

Fig. 8 XRD patterns of (a) $AmAc_1$-NCs and (b) $AmAc_2$ NCs.

geometry of the DPEA molecules and its specific hindrance that induces a preferential surface affinity for nanocrystals leading to the formation of rods. The exact driving force behind the formation of nanowires is the partial steric hindrance of the two biphenyl groups close to the nanoparticle surface and an affinity of this molecule to attack a preferential face of the starting nanocrystal that induces the formation of the nanorods. Indeed, we see that with DPPA, which contains an additional methylene group (propyl group DPPA molecule) between the biphenyl part and the amine, the nanocrystals are cubic type like the others, while with one methylene group (methyl group, DPMA molecule), there is no cutting of the starting nanocrystals and the solution is totally unstable.

The second time, the hindrance around the amino group is increased with the two last TPMA and DPMA molecules. In both molecules, the amino function is hindered without being directly linked to the aromatic group. In both cases, when the pre-SB solution containing TPMA and DPMA molecules is dropped into SA solution, the SB solution is first yellow transparent, turns orange after a few seconds, then turbid in a few minutes before precipitation occurs after a few hours. TEM copper grids have been prepared during the first few minutes of the reactions. For DPMA (Fig. SI-36†), we observe the formation of nanorods but they are larger than those observed with DPEA, along with some unchanged PVK-TOA nanocrystals. For TPMA (Fig. SI-37†), the nanocrystals remained unchanged from the starting solution. So, with these two molecules, we reach the limit of our process in terms of the nature of AAA molecules. The steric hindrance around the amine function has a negative impact and with higher hindrance like with TPMA molecules, the starting PVK-TOA-NCs remain unchanged and no cutting process is detectable.

In XRD analysis, all nanocrystals obtained with this series exhibit monoclinic structures (Fig. SI-27† for MPMA-NCs, SI-28 for MPEA, SI-30 for DPEA-NCs, SI-34 for DPPA-NCs, SI-36 for DPMA and SI-37† for TPMA). Concerning the photoluminescence studies, DPMA, TPMA, and MPMA (Fig. SI-4†) show a slight red shift to 522 nm and a large FWMH (FWHM >19 nm), due to the presence of aggregates and the lack of stability in solution. The presence of these aggregates is also confirmed with the measurement of PLQY. TPMA-NCs and DPMA-NCs have the worst values, at 5% and 8% respectively, whereas MPMA-NCs and DPEA-NCs show values of 41% and 45%, respectively. On the other hand, the DPPA-NCs and MPEA-NCs, their more stable solutions just after the synthesis, exhibit good PLQY values of 70% and 64%, respectively.

2.2.4 Fourth series with amino acid molecules. Finally, we tried two amino acid molecules, $AmAc_1$ and $AmAc_2$, to evaluate the influence of the carboxylate group close to the amino function, during the MLARP process. Carboxylate groups are well-known to stabilize nanocrystals and to ensure bonding with nanocrystals.[24–28] For both molecules, when pre-SB solutions are added, the color of SA solutions changes from yellow to orange, and becomes turbid in both cases and this process is faster with the $AmAc_1$ molecule.

When pre-SB contains $AmAc_1$, TEM observations show for the final SA solution a modification of the starting materials with the formation of nanosheet structures similar to the tetragonal phase of $CsPb_2Br_5$ nanosheets (Fig. 7a).[60,61] When $AmAc_2$ is used, TEM observation highlights the cutting of PVK-TOA as for other AAA molecules. But, in HAADF-STEM, we showed areas still in the slicing process (Fig. 7b), with larger original nanocrystals not completely cut.

For $AmAc_1$-NCs, the XRD pattern exhibits the tetragonal phase structure of $CsPb_2Br_5$ nanosheets (Fig. 8a), with the main line at 11.72° and secondary line at 23.48° (respectively (002) and (210) planes, reference PDF#25-0211),[45,50,60,62–64] while $AmAc_2$-NCs exhibit an orthorhombic structure (Fig. 8b).

Regarding the photoluminescence studies, like the previous series a similar redshift is observed, 517 nm for $AmAc_2$-NCs (FWHM ≈18 nm) and 519 nm for $AmAc_1$-NCs (FWHM >19 nm). PLQYs are in agreement with these values, with a poor value for $AmAc_1$-NCs, only 19%, and 40% for $AmAc_2$-NCs. For $AmAc_1$-NCs, this result is certainly due to the modification of the morphology of the nanocrystals to yield pallet structures and its lower stability and the aggregation of these pallets in solution. We could expect a better result with $AmAc_2$-NCs because we obtained apparent nanocubes like other nanocrystals and also a better functionalization of the surface with a –COOH and $–NH_2$ group. However, this low value reflects probably the presence of aggregates in the

solution, as well as poor nanocrystal cutting as observed in HAADF-STEM.

Thus, the proximity of the –COOH group to the NH_2 function in $AmAc_1$-NCs has a real impact on the topology of the final nanocrystals. This result is certainly caused by a better complexation of the $AmAc_1$ molecule with the lead(II) cation, compared to the $AmAc_2$ molecule, leading to a complete structural modification of the final nanocrystals. For the $AmAc_2$ molecule, this complexation appears to be inoperative, and unlike other AAAs, the presence of the –COOH group seems to be a disadvantage for the cutting process. But, in both cases, in contrast to previous methods reported in the literature which employed the hot injection method with amino acids, resulting in nanocrystals with excellent stability and high PLQY values, we emphasize here that neither of the AmAc molecules used in our study is suitable for the MLARP process.[65,66]

2.3 Highlighting the PbO structure and Pb° nanoparticles during the MLARP process

TEM observations show, for a large number of samples, the formation of Pb° nanoparticles (Pb°-NPs) onto the surface of the nanocrystal. They are commonly observed in the literature for

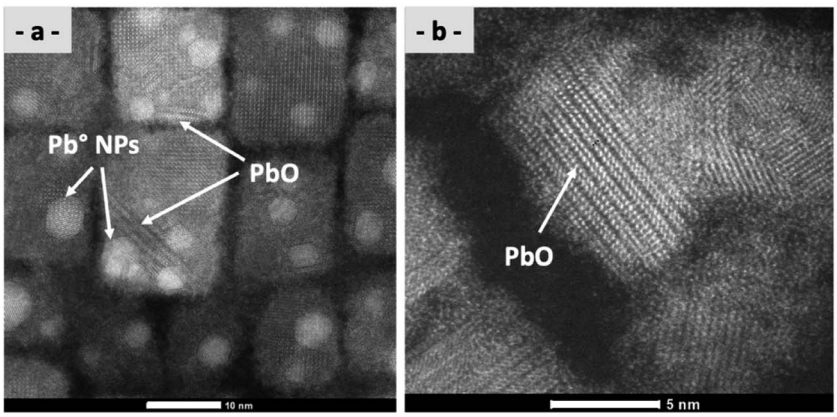

Fig. 9 HAADF-STEM analysis of DPPA to highlight (a) Pb°-NP and PbO nanoribbon structures (scale bar 10 nm) and (b) assembly of PbO nanoribbon structures (scale bar 5 nm).

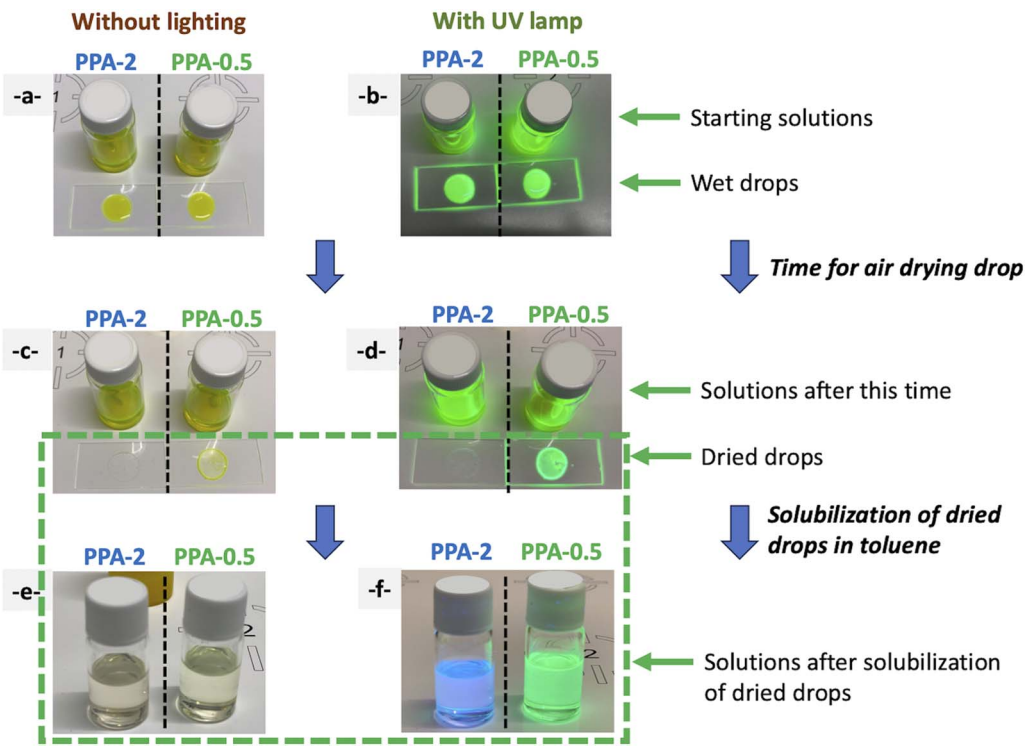

Fig. 10 Sample SB solutions of PPA-NCs: (a) view of the solutions and the drops of PPA-2-NCs (ratio of $PPA/Pb^{2+} = 2$) and PPA-0.5-NCs (ratio of $PPA/Pb^{2+} = 0.5$), (b) lighted with a UV lamp, (c) showing the drying of a drop-in glass slide, (d) lighted with a UV lamp, (e) both solutions obtained by dissolution in toluene of both dried drops onto the glass slide and (f) lighted with a UV lamp.

$CsPbBr_3$ nanocrystals. Several contradictory explanations have been given for the presence of these Pb° NPs, in particular their formation during the TEM observation with the electronic beam.[67,68] In our case, with our STEM, a contrary observation has been observed: the disappearance of Pb° NPs with an electronic beam (see Fig. SI-41†). Recently, Lee and colleagues reported an interesting explanation for the presence of lead nanoparticles during the synthesis of perovskites.[69] For them, the defects in the surface and core within $CsPbBr_3$ nanocrystals can distort the perovskite structure, resulting in the intrinsic instability of perovskite nanocrystals. The defects carry a small negative or positive charge, which induces the oxidation (forming PbO_2) or reduction (forming Pb°) of oppositely charge atoms due to charge neutrality under ambient conditions.[70] The oxidation and reduction reactions predominantly occur in the surface and core regions of the perovskite nanocrystals, respectively.

In our case, we observe the presence of Pb° NPs on the nanocrystal's surfaces (Fig. 9a), but in some cases, we observe also the presence of PbO ribbons (Fig. 9b). We can attest to their presence by the perfect matching between our ribbons and the crystal structure of PbO (Fig. SI-42 and SI-43†).[71] As previously described, the reduction of Pb^{2+} within $CsPbBr_3$-NCs in Pb° nanoparticles is due to halide vacancies acting as electron traps, which can facilitate their reduction.[49] In our study, this reduction process and the formation of PbO structures under ribbon form are visible after the cutting process and not every time.

These PbO structures are certainly due to the liberation of the Pb^{2+} cation in solution during the cutting process and the presence of oxygen in solution. These structures had not previously been described in the literature, since synthesis took place in a glovebox without the presence of dioxygen. Interestingly, the reduction phenomena are limited when the nanocrystals are very well calibrated, particularly with AAA having a methylene group instead of an ethylene group-like linker between the amine function and the phenyl group. So, it seems that the formation of Pb°-NPs and PbO ribbons is dependent on the reactivity of AAAs with the starting nanocrystals (PVK TOA). If the reactivity is very efficient, their formation is reduced, but if the reactivity of AAA is less efficient, combined with the synthesis conditions, the formation of Pb°-NPs and PbO ribbons is more visible. This hypothesis is corroborated by our TEM observations and at the experimental level with the samples giving very stable and non-aggregated nanocrystals such as *t*BuPMA-NCs, MeOPMA-NCs, or PMA-NCs.

Hence, our procedure can be carried out under standard temperature conditions without the need for a glovebox, but enhancements can be achieved by using a high-quality anhydrous solvent to avoid the presence of PbO structures. However, even these PbO ribbons are not expected; to our knowledge, such nanostructures have not been described in the literature.

2.4 Impact of the AAA/Pb^{2+} ratio in solution and on glass plates

For a couple of samples, under similar synthesis conditions, we observed that during the preparation of the XRD sample and the drying process on the glass plate, the drop became colorless and not emissive. On the other hand, this was the case with all AAA

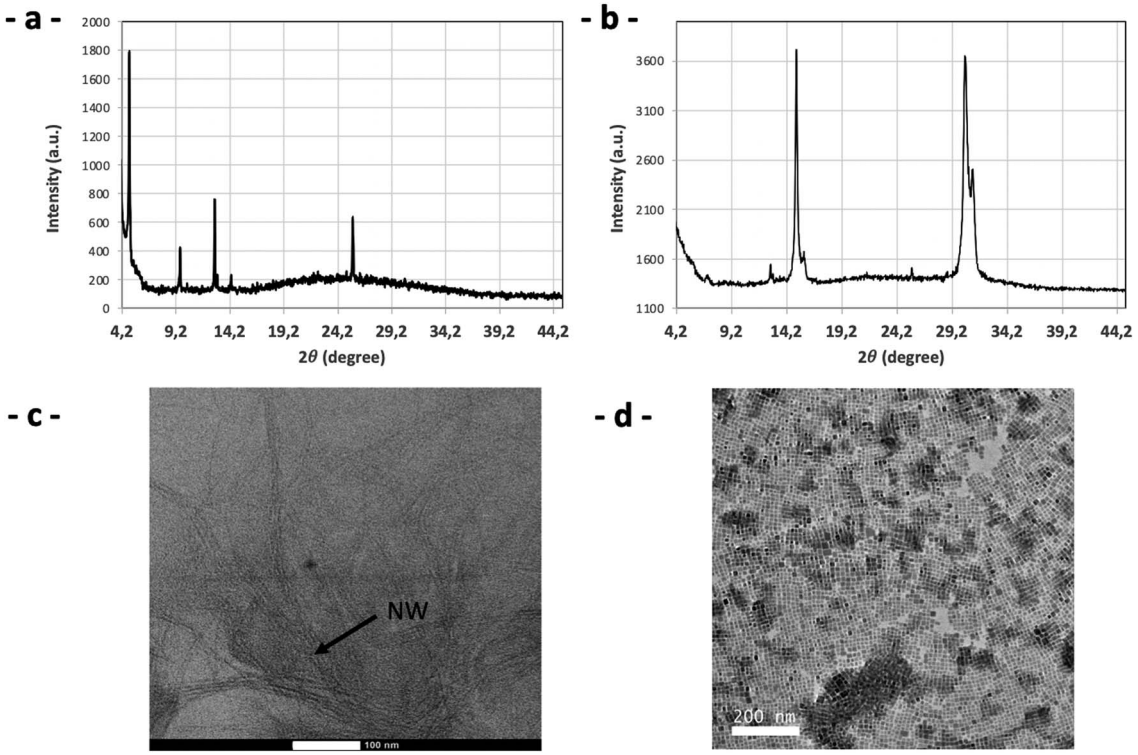

Fig. 11 XRD of a dried drop of (a) PPA-2 and (b) PPA-0.5 and corresponding pictures of (c) HRSTEM (scale bar 100 nm) of a dried drop of PPA-2 samples dissolved in toluene, with narrow nanowires, and (d) TEM (200 kV, scale bar 200 nm) of PPA-0.5 showing PPA-nanocrystals.

molecules when AAA was added with a ratio of AAA/Pb^{2+} greater than 1. So, following these observations and to analyze the effect of the AAA/Pb^{2+} ratio on the final nanocrystals, we used PPA molecules as a probe to understand the influence of AAA molecules on this MLARP process.

Two sets of PPA–SB solutions have been prepared, one with a ratio of PPA/Pb^{2+} = 2 (PPA-2) and a second at 0.5 (sample PPA-0.5). Both yellow solutions have a similar appearance and present a green emission under UV light (Fig. 11a and b). Then both solutions are dropped on two different glass plates. The two drops from PPA-2-NCs and PPA-0.5-NCs solutions present a green emission under UV light before their drying (Fig. 10a and b).

Although both solutions remain unchanged during the drying time of both drops with a green emission for both of them, the dried drop from sample PPA-2-NCs is colorless (with a slight blue emission) while the dried drop sample from PPA-0.5-NCs remains yellow with a green emission (Fig. 10c and d).

Then, the two residues from the PPA-2-NCs dried drop and the PPA-0.5-NCs dried drop are re-solubilized in toluene. The resulting solution presents a blue emission for sample PPA-2-NCs while PPA-0.5-NCs exhibit a green emission (Fig. 10f).

The XRD analysis for PPA-2-NCs (dry sample, PPA/Pb^{2+} = 2) could be assimilated to nanowire structures like RP structures with a main line at 4.83° (Fig. 11a). This result is corroborated in TEM with the presence of nanowires (Fig. 11c). These two analyses are in agreement with nanowire structures already observed previously by Kostopoulou *et al.* and look like hair.[72]

For PPA-0.5-NCs (ratio of PPA/Pb^{2+} = 0.5), XRD analysis (Fig. 11b) and TEM (Fig. 11d) are in agreement with previous PPA-nanocrystals. So, for a lower ratio of PPA/Pb^{2+} ≈0.5, the drying of the drop doesn't induce structural modification of nanocrystals. A higher ratio modifies drastically the structure of nanocrystals during the drying of the drop. The cutting process

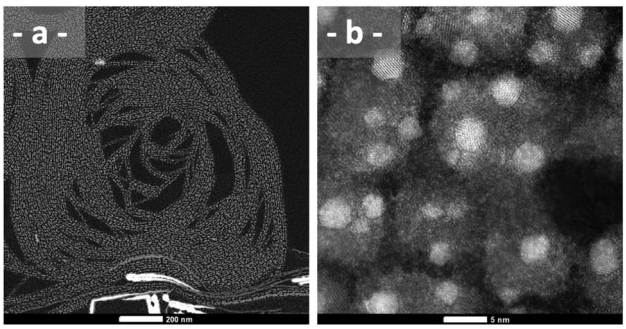

Fig. 12 TEM pictures of samples obtained (a) with PEA molecules with a ratio of PEA/Pb^{2+} = 4 showing nanowires (scale bar 200 nm) and (b) with DPPA/Pb^{2+} = 2, showing undefined nanocrystals without Cs^{+} cations (scale bar = 5 nm) with Pb° nanoparticles.

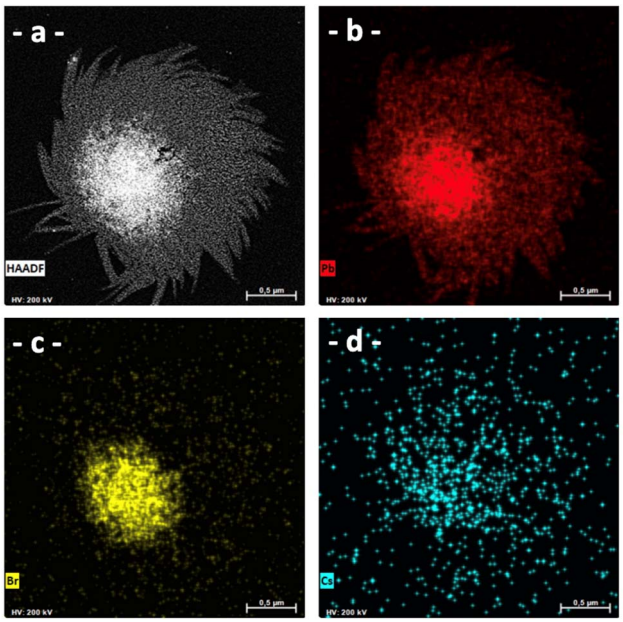

Fig. 13 HAADF-STEM analysis of PEA (ratio of PEA/Pb^{2+} = 4) (a) in HAADF and by EDS to visualize (b) Pb element; (c) Br element; and (d) Cs element.

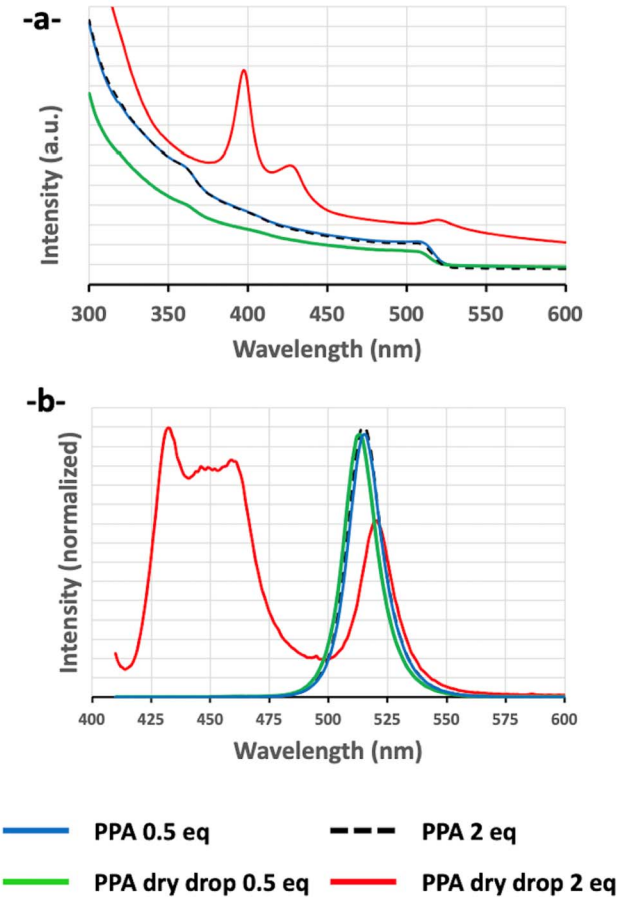

Fig. 14 Optical spectroscopy of PPA-nanocrystals in two different ratios: PPA-2 (ratio of PPA/Pb^{2+} = 2) and PPA-0.5 (ratio of PPA/Pb^{2+} ≈0.5); (a) absorption spectra of solutions from, in a dotted black line, 2 eq. of PPA before drying, in a red line, after drying of the drop, in a blue line, 0.5 eq. of PPA before drying, and in a green line, after drying of the drop; and (b) emission spectra (excitation at 403.5 nm) of solutions from, in a dotted black line, 2eq. of PPA before drying, in a red line, after drying of the drop, in a blue line, 0.5 eq. of PPA before drying, and in a green line, after drying of the drop.

by PPA molecules continues to act during drying, due to the excess of PPA molecules and its increasing concentration in the final drop.

The formation of these nanowires has also been observed with a higher ratio of AAA/Pb^{2+} ($\geq$2). For example, with a ratio of PEA/Pb^{2+} = 4, similar nanowires have been observed by HAADF-STEM (Fig. 12a). As another example, with DPPA-NCs, by HAADF-STEM, for a ratio of DPPA/Pb^{2+} = 2, undefined nanocrystals without Cs^+ cations (scale bar = 5 nm) with Pb° nanoparticles are observed (Fig. 12b). These last undefined structures with cubic like appearance seem to be intermediate structures between the well-defined nanocrystals of $CsPbBr_3$ and the ultimate broken structure, the nanowires.

Through EDS, we can observe that this type of structure is composed solely of lead and bromine atoms and contains very few cesium cations (Fig. 13).

These results are confirmed by optical spectroscopy. The absorption and the emission bands of PPA-0.5-NCs (ratio of PPA/Pb^{2+} = 0.5) are similar before and after drying (Fig. 14). This result confirms a structural conservation of nanocrystals during the drying process. Meanwhile, for PPA-2-NCs (ratio of PPA/Pb^{2+} = 2), the optical results drastically changed before and after the drying process. Indeed, before the drying process, PPA-2-NCs (ratio of PPA/Pb^{2+} = 2) present an absorption and emission similar to PPA-0.5-NCs (ratio of PPA/Pb^{2+} = 0.5). However, after drying, the absorption band confirms the structural modification of nanocrystals in different structures, with an absorption band characteristic of Ruddlesden–Popper structures (n = 2, 400 nm, and n = 3, 430 nm) and $CsPbBr_3$ nanocrystals (Fig. 14). The emission bands reflect the absorption spectroscopy, with two emission zones, one between 420 and 460 nm[73–75] (for RP structures) and one at 520 nm (for $CsPbBr_3$ nanocrystals) (Fig. 14).

Thus, a weaker ratio (ratio of PPA/Pb^{2+} = 0.5) avoids an alteration of nanocrystals during the drying process while a stronger ratio (ratio of PPA/Pb^{2+} = 2) induces a structural modification of the nanocrystals. So, with an excess of AAA, the previous PVK-TOA-NCs are cut in nanocrystals first and the process is extended to the formation of RP structures, until the

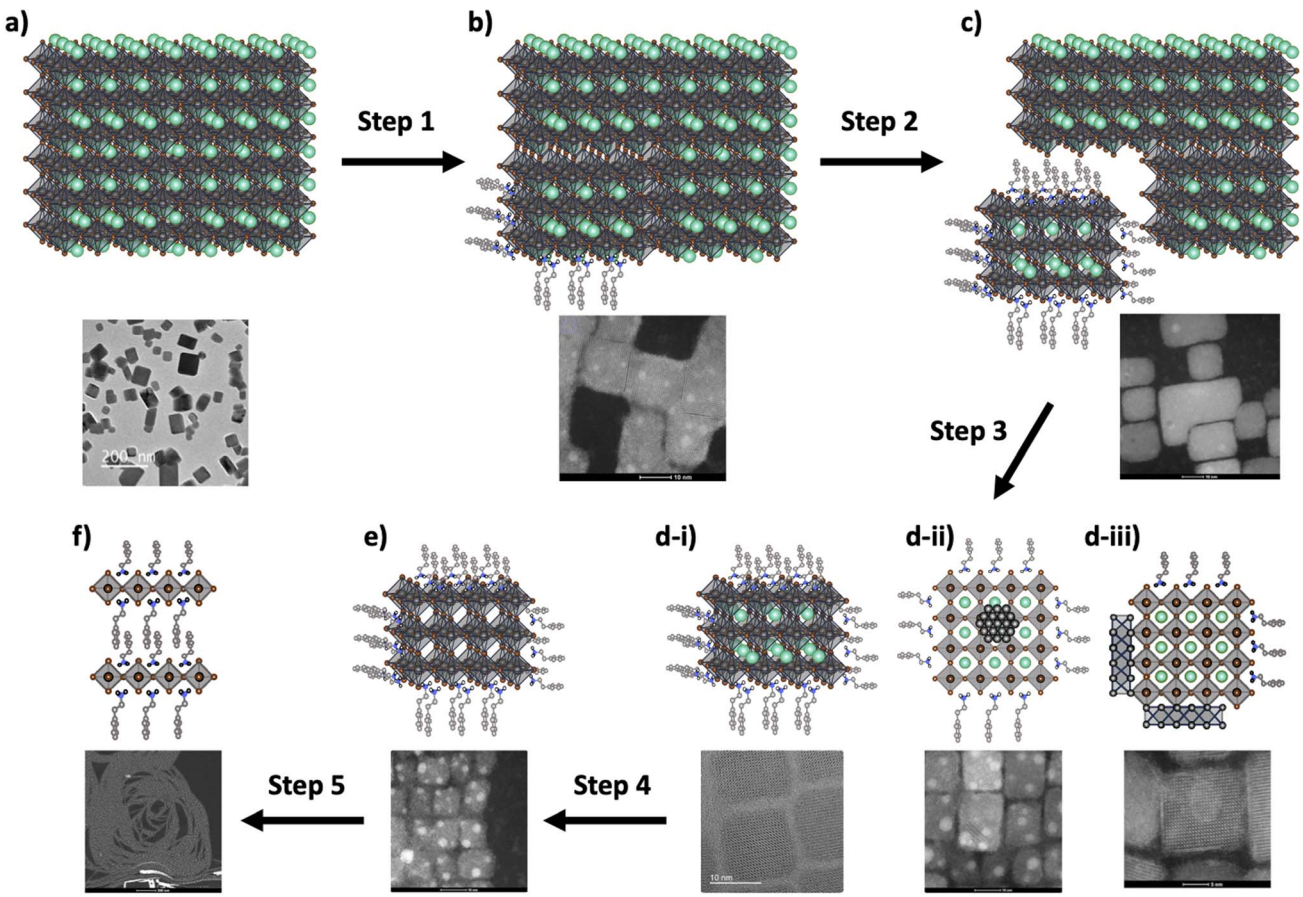

Scheme 4 Scheme of the mechanism occurring during the MLARP process, with the corresponding TEM pictures, (a) PVK TOA used first (scale bar 200 nm), (b) first action of AAA with some crystallographic lines without the Cs^+ cation showing the cutting process (scale bar 10 nm), (c) detachment of new calibrated nanocrystals (scale bar 10 nm), and schematic representation of different structures of nanocrystals detected after this process with ((d)-i) representation of calibrated nanocrystals (scale bar 10 nm), ((d)-ii) similar nanocrystals with the presence of Pb° nanoparticles (scale bar 10 nm), and ((d)-iii) similar nanocrystals with the presence of PbO ribbons on the nanocrystals (scale bar 5 nm); (e) when AAA is in excess some undefined nanocrystal without Cs^+ is formed (scale bar 10 nm) and (f) formation of ultimate nanowires due to AAA in excess (scale bar 200 nm).

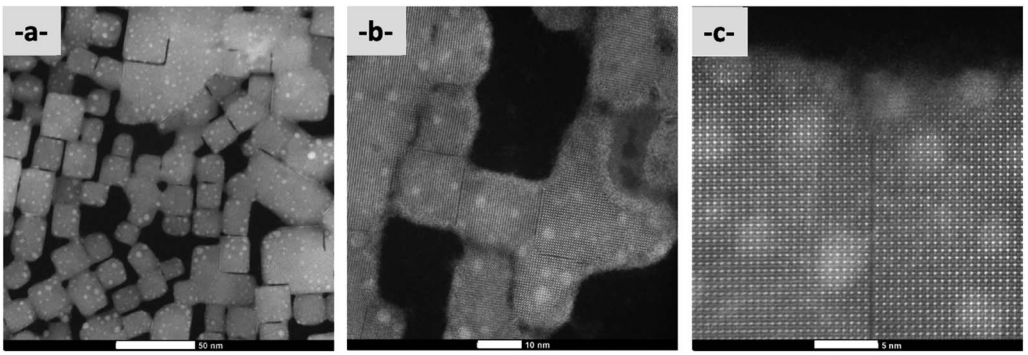

Fig. 15 HAADF-STEM of PEA nanocrystals (ratio of PEA/Pb^{2+} = 1) dropped on the copper grid after less than one minute of the addition of pre-SB solution, showing the different cutting areas, (a) scale bar 50 nm, (b) scale bar 10 nm and (c) scale bar 5 nm.

final degradation of nanocrystals, during this drying process, helped by the increase of AAA molecule concentration.

In conclusion, the ratio of AAA/Pb^{2+} has to be controlled to ensure a good cutting of previous PVK-TOA-NCs in solution, without affecting these final nanocrystals during their drying for their observations by XRD analysis. However, even if we have seen for PPA-NCs a ratio close to 0.5 is enough for a good cutting, for others AAA molecules, this ratio could be not sufficient to get it. Thus, the compromising ratio between 0.5 and 1, depending on AAA molecules, is adequate. Beyond this ratio, the cutting process continues to occur and can take place either directly in the solution or during the solution drying (as for XRD analyses), where the amine concentration increases and this cutting process continues.

2.5 Effect of AAA molecules on the mechanism occurring within the MLARP process

The effect of AAA molecules on the mechanism occurring within the MLARP process has been followed by HR-STEM and by experimental compilation of all TEM results. This study shows that AAA plays a fundamental role in the breakdown of PVK-TOA-NCs, as depicted in Schemes 4a and b. This modification is due to AAA's coordination with lead(II) surface cations, resulting in the production of smaller and highly calibrated nanocrystals, as shown in Schemes 4(b)–(d-i).

Fig. 15 depicts the initial moments of the organic molecule cutting of the starting PVK-TOA-NCs, with the observation of the cutting zones. The side of the crystals is also less well-structurally defined, showing a kind of cloud of lightweight atoms such as carbon, indicating the presence of organic matter. However, it is important to note that during this process, certainly due to the inherent characteristics of the nanocrystal surface defects, some additional structures appear in the solution, including Pb^{0} nanoparticles (Scheme 4d-ii) and PbO ribbon structures (Scheme 4d-iii). Moreover, this process can continue to progress with an excess of AAA, ultimately leading to the formation of a cubic structure devoid of Cs^{+} cations, as illustrated in Scheme 4e. Finally, under these conditions, nanowires composed of lead resembling RP structures are observed, as shown in Scheme 4f.

The action of AAA molecules does not only limit the cutting of the initial nanocrystals but also influences their nature, their stability in solution, and their tendencies to aggregate. Thus, even if most of the AAA molecules tend to form highly calibrated cubic nanocrystals, some rods can be designed depending on the hindrance of AAA molecules, with DPEA or some nanosheets like with $AmAc_1$. But if this hindrance is too much this process doesn't occur, as with TPMA and DPMA molecules. Independently of the calibration of the final nanocrystals, the nature and particularly the topology of the molecule play a fundamental role in their stability in solution.

3 Conclusion

Recently, based on the modified LARP method, we have designed high-calibrated nanocrystals of $CsPbBr_3$ by soft chemistry, in an easy process, with the help of phenylethylamine (PEA) molecules. Similarly to hybrid 2D-perovskites,[78] and to perovskite films[79] in which the organic molecules can play a great role in the chemical structures and the optical properties of these hybrid materials, the study of the influence of organic molecules on the functionalization of $CsPbBr_3$ nanocrystals by AAA molecules was interesting to investigate for potential uses in OLEDs or photovoltaic devices.

To our knowledge, only a few AAA molecules have been studied but by HI method, like PEA or recently DPPA.[80] In this paper, we have investigated a large topology of these AAA molecules by this new modified LARP method, that occurs by soft chemistry.

We highlight a specific mechanism for cutting submicron crystals into nanocrystals. Thanks to HAADF-STEM and optical spectroscopy, we have followed this mechanism during this new MLARP process for all types of aryl-alkylamine molecules. The different steps of this mechanism have been proposed. It has been shown that this process can be controlled by the amine concentration. A ratio between 0.5 and 1, dependent on AAA, is a good compromise to get stable nanocrystals and analyze them without damage. Ultimately, with a higher ratio (AAA/Pb^{2+} >1), helped with a higher concentration, the complete degradation of the initial submicron crystals in a structure similar to Ruddlesden–Popper structures can be achieved.

We have shown the presence of AAA molecules on the nanocrystal surface, and the efficient functionalization of nanocrystals with the probe molecules, through CF_3–PEA or baclofen molecules. We have seen that only the methylene group is sufficient to properly functionalize the $CsPbBr_3$ nanocrystals' surface and to highly calibrate them. We showed that the nature of aryl-alkylamine has a real impact on the size calibration, structure (monoclinic, rhombohedral, or tetragonal), shapes (cubes, nanorods, nanosheets) of nanocrystals and on their stability in solution. This stability is also deducible by photoluminescence studies and the PLQY values. When the nanocrystals are stable in solution and present a high calibration, without the presence of micro-aggregates in solution, the PL presents a low FWMH with a good PLQY.

Thus, the photoluminescence of the samples is directly correlated with the stability or aggregation state of the nanocrystals in solution, which has an impact on the quantum yield of the sample rather than the wavelength of the sample. Within the same series, the emission wavelength is almost the same after synthesis. The quantum yields are significantly higher if the nanocrystals are well-calibrated in size and do not induce aggregation states in solution. The photoluminescence will tend towards longer wavelengths with a broader emission band and a decrease in quantum yield when the solution becomes unstable and the nanocrystals aggregate. This observation has been detected particularly with heterocyclic or polyaromatic systems. About photoluminescence lifetimes, summarized in Table 1 and developed in Table SI-2,† every sample exhibited multi-exponential decays. The decay curves can be well-fitted by a triexponential function, where α_1, α_2, and α_3 are the relative amplitudes of each component (in %), and τ_1, τ_2, and τ_3, with $\tau_3 > \tau_2 > \tau_1$ being the temporal components. By examination of lifetime values for every sample, we can observe quite similar values of τ_1, τ_2, and τ_3 and a better relative amplitude for α_2 and α_3. These three components can be explained by different hypotheses like a distribution size not fully homogeneous or due to different defects and state surfaces. These photoluminescence lifetime results confirm also the TEM observations because nanocrystal samples exhibit a relatively similar distribution size and shape and the anchorage point from the organic molecule is similar (the $-CH_2-NH_2$ group coordinates to the NC surface). Only $AmAc_1$ exhibits two exponential decays in agreement with a different structure compared to other samples.

Finally, this work promotes the new modified-LARP method to obtain highly calibrated functionalized $CsPbBr_3$ nanocrystals with large panels of AAA. These AAA-NCs are potentially promising for OLED applications because we can obtain well-calibrated NCs by soft chemistry and an easy way compared to other methods and also particularly with aryl molecules having a donor group like MeO–PMA or *t*Bu–PMA molecules, that presented a high PLQY of 78 and 81% respectively (Tables 1 and SI-2†). So, this high calibration of functionalized perovskite nanocrystals is a promising result for inkjet printer applications because they can self-assemble automatically during their deposit as we can observe on a copper grid where the surface is fully covered by NCs.

In conclusion, this new modified LARP method opens the way for the use of optically active π-conjugated organic molecules and enlarging to other $CsPbX_3$-type nanocrystals.

4 Experimental details

4.1 Materials

Lead(II) bromide ($PbBr_2$, 99.99%), cesium carbonate (Cs_2CO_3, 99.99%), oleic acid (OA, 90%), dimethylformamide (DMF, 99.8% anhydrous), toluene (≥99.9%), tetra-octylammonium bromide (TOABr, 98%), 1-naphthylmethylamine (Naph–PMA, $C_{11}H_{11}N$, 97%), 4-phenylbenzylamine (PPMA, $C_{13}H_{13}N$, >97%), and 4-*tert*-butylbenzylamine (*t*Bu–PMA, $C_{11}H_7N$, >98%) were sourced from Sigma-Aldrich. Phenylethylamine (PEA, $C_8H_{11}N$, ≤100%), benzylamine (PMA, C_7H_9N, 99%), 4-methoxybenzylamine (MeO–PMA, $C_8H_{11}NO$, 98%), 4-(trifluoromethyl)benzylamine (CF_3–PMA, $C_8H_8F_3N$, >98%), 3-phenylpropylamine (PPA, $C_9H_{13}N$, >97%), 3,3-diphenylpropylamine (DPPA, $C_{15}H_{17}N$, >98%), 2,2-diphenylethylamine (DPEA, $C_{14}H_{15}N$, >98%), 2-methyl-2-phenethylamine (MPEA, $C_9H_{13}N$, >98%), homophenylalanine ($AmAc_1$, $C_{10}H_{13}NO_2$, >98%), baclofen ($AmAc_2$, $C_{10}H_{12}ClNO_2$, >98%), 2-(4-methoxyphenyl)ethylamine (MeO-PEA, $C_9H_{13}NO$, >98%), 2-(4-trifluoromethylphenyl)ethylamine (CF_3–PEA, $C_9H_{10}F_3N$, >98%), 2-(aminomethyl)thiophene (ThioMA, C_5H_7NS, >98%), 2-(2-aminoethyl)thiophene (Thio–EA, C_6H_9NS, >98%), triphenylmethylamine (TPMA, $C_{19}H_{17}N$, >95%), benzhydrylamine (DPMA, $C_{13}H_{13}N$, >97%) and 1-phenylethylamine (MPMA, $C_8H_{11}N$, >98%) were sourced from TCI-Chemicals.

4.2 Synthesis

In the MLARP method, a fresh toluene solution containing larger preformed $CsPbBr_3$ nanocrystals stabilized by tetraoctylammonium salt (TOA^+) and free of AAA is prepared. This solution called SA is prepared by mixing Cs_2CO_3 in oleic acid (leading to the formation of cesium oleate (CsOA)) with a toluene solution of lead bromide and TOABr.[76,77] This last one plays the role of transfer agent for the $PbBr_2$ salt in toluene (formation of $[PbBr_4]_2(TOA)_2$) and contributes to $CsPbBr_3$ nanocrystal stabilization in toluene. To improve the quality of the final nanocrystals the mixture of $[PbBr_4]_2(TOA)_2$ in toluene is cooled at 0 °C. When CsOA in OA is added to $[PbBr_4]_2(TOA)_2$ in toluene, the solution becomes yellow-green and this transparent mixture becomes a turbid yellow-green. Then, PVK-TOA nanocrystals were recovered after centrifugation at 10 000 rpm for 20 min, at 5 °C, and redispersed in toluene (10 mL, solution SA).

In parallel, a pre-SB solution is synthesized with the help of two mixtures. The first is a solution of $PbBr_2$ and OA (with the ratio of $OA/Pb^{2+} \approx 4$) in DMF, at room temperature (0.1 M in Pb^{2+}). The second one contains Cs_2CO_3 and OA in DMF ($OA/Pb^{2+} \approx 4$, $Cs^+/Pb^{2+} \approx 0.5$). The two mixtures were stirred at 35 °C for at least 10 min to ensure the complete dissolution of all materials. We use the same ratio between these reagents to keep the stochiometric ratio unchanged between Pb^{2+}, OA, and Cs_2CO_3 in pre-SB compared to SA. Just before mixing pre-SB and

SA, AAA is added last in pre-SB. The amount of AAA is adjusted depending on the reactivity of the molecule used to get the better stability of the final SA solution (see Table SI-1†). Then, the final pre-SB (2.5% in volume of SA) is dropped to SA at room temperature to give a clear transparent solution of the final monodisperse perovskite-nanocrystals (SB solutions, Scheme 2), without other treatments.

4.3 Characterization

Nanocrystals were observed and analyzed by transmission electron microscopy with a JEM 2100 Plus microscope (JEOL) and an accelerating voltage of 200 kV. High-resolution TEM (HRTEM) and high-angle annular dark field scanning TEM (HAADF-STEM) images, and energy dispersive X-ray spectroscopy (EDS) measurements were taken with a Titan G2 80-300 microscope (ThermoFisher Scientific) operating at 300 kV. The XRD experiments were performed on a Malvern Panalytical Aeris Research Edition, with a sample changer of 6 positions and a PIXcel 1D detector. The working power is 300 W (30 kV–10 mA). The used radiation is copper Kalpha1 + 2 (approx. 1.5406 angstrom). Samples were placed on a Si (510) sample holder to reduce background. Data were measured from 2 to 60° in 2θ with a total scan time of 10 min per scan with a rotation of the sample during acquisition. The UV–vis absorption spectra of nanocrystals were recorded using a UV–vis spectrometer (PerkinElmer LAMBDA 950 UV/vis/NIR spectrophotometer) in the wavelength range from 300 to 700 nm. Emission and decay time-based measurements were registered using an Edinburgh Instruments FS5 spectrofluorometer on the principle of the steady-state mode and the time-correlated single-photon counting (TCSPC) mode, respectively. The lifetime decay was measured with the module EDEDEPL-405 (405 nm ($\pm$5 nm) picosecond pulsed diode laser, typical pulse width: 60 ps @ 10 MHz, rep rate: 20 kHz–20 MHz) coupled with an FS5 spectrofluorometer. The internal quantum efficiencies of nanocrystals were quantitatively determined using an integrating sphere-equipped spectrofluorometer (FS5, Edinburgh). Fluorescence excitation and emission spectra, and quantum yield values were obtained using an Edinburgh Instrument FS5 fluorescence spectrometer. The spectra were recorded in right angle mode using quartz cuvettes with a 1 cm path length. The fluorescence quantum yield values were obtained using the integrating sphere sample cassette available for the FS5 spectrometer. The Fluoracle software was used to calculate the absolute quantum yield values by comparing the blank and the sample spectra.

4.3.1 Optical absorption studies. Absorption spectra of all nanocrystals present an excitonic resonance absorption peak around 510 nm, in agreement with shape-pure $CsPbBr_3$ nanocube samples exhibiting only slight differences in the UV-vis absorption spectral fingerprint depending on the nature of AAA: excitonic peak centred at 508–509 nm for aryl-PMA nanocrystals (Fig. SI-37 and 38†),[15,60] 510 nm for aryl-PEA nanocrystals, 512 nm for AA1 and AA2 (Fig. SI-38†), and 513 nm with a sharper excitonic resonance absorption peak at 513 nm for DPEA (Fig. SI-38†). For MPMA, DPMA, and TPMA-based nanocrystals (Fig. SI-38†), a more diffuse band is observed, due to solution turbidity and aggregates in solution, and their wider excitonic peak is centered at 516 nm.

4.3.2 Photoluminescence lifetime. All dispersions exhibited multi-exponential decays. The decay curves can be well-fitted by a triexponential function, where α_1, α_2, and α_3 are the relative amplitudes of each component (in %), and τ_1, τ_2, and τ_3, with $\tau_3 > \tau_2 > \tau_1$ are the temporal components. A triexponential fit of the decay profiles gave acceptable values of residuals and chi-squares ($\chi 2$). Table SI-2 and Fig. SI-6† give the details of the percentage of the constant, decay time, and average lifetime. The radiative constant (k_r) and non-radiative constant (k_{nr}) are rates that give further insight into the charge carrier recombination processes where the k_r/k_{nr} value for $CsPbBr_3$ nanocrystals is for most of the components greater than 1.7 and can reach 4, in line with the PLQY values of the systems (Table SI-2†). The three τ_i values are between 1 and 40 ns but with the third main component around 35–40 ns. These values are close to those found in the literature for triexponential fit, with $\tau_{average}$ of around 18 ns (Fig. SI-28†).[36,45,81,82]

Author contributions

C. R. Mayer: conceptualization; methodology; supervision; investigation; writing – original draft/review/editing/funding acquisition; H. Levy-Falk: investigation; G. Trippé-Allard: investigation; N. Guiblin: XRD investigations; F. Fossard: investigation by HR-TEM and EDS; M. Vallet: investigation by TEM; Jean-Sébastien Lauret: review/funding acquisition and Emmanuelle Deleporte: review/funding acquisition.

Conflicts of interest

There are no conflicts to declare.

Acknowledgements

The authors acknowledge financial support from the LABEX Charmmmat (University Paris-Saclay), Agence Nationale de la Recherche: EMIPERO Project ANR-18-CE24-0016 and 2D-HYPE: ANR-21-CE30-0059. The work of H. Levy-Falk is supported by Agence de l'Innovation de Défense. The HAADF-STEM study was carried out within the MATMECA consortium, supported by the ANR-10-EQPX-37 contract, and has benefited from the facilities of the Laboratory MSSMat (UMR CNRS 8579), CentraleSupélec.

References

1 Q. J. Huang and Y. Zhu, *Adv. Mater. Technol.*, 2019, **4**, 1800546.
2 Q. Zhang, Q. Shang, R. Su, T. Thu Ha Do and Q. Xiong, *Nano Lett.*, 2021, **21**, 1903–1914.
3 Y. Wang, L. Song, Y. Chen and W. Huang, *ACS Photonics*, 2020, **7**, 10–28.
4 W. Shen, J. Chen, J. Wu, X. Li and H. Zeng, *ACS Photonics*, 2021, **8**, 113–124.

5 E. Mohammed, S. Al-Qaisi, Z. A. Alrowaili, M. Alzaid, E. Maskar, A. Es-Smairi, T. V. Vu and D. P. Rai, *Sci. Rep.*, 2021, **11**, 20622.
6 S. Wang, A. A. Yousefi Amin, L. Wu, M. Cao, Q. Zhang and T. Ameri, *Small Struct.*, 2021, **2**, 2000124.
7 X.-K. Liu, W. Xu, S. Bai, Y. Jin, J. Wang, R. H. Friend and F. Gao, *Nat. Mater.*, 2021, **20**, 10–21.
8 L. N. Quan, B. P. Rand, R. H. Friend, S. G. Mhaisalkar, T.-W. Lee and E. H. Sargent, *Chem. Rev.*, 2019, **119**, 7444–7477.
9 A. Ren, H. Wang, W. Zhang, J. Wu, Z. Wang, R. V. Penty and I. H. White, *Nat. Electron.*, 2021, **4**, 559–572.
10 C. K. Ng, C. Wang and J. J. Jasieniak, *Langmuir*, 2019, **35**(36), 11609–11628.
11 Y. Bekenstein, B. A. Koscher, S. W. Eaton, P. Yang and A. P. Alivisatos, *J. Am. Chem. Soc.*, 2015, **137**, 16008–16011.
12 Z.-K. Tan, R. S. Moghaddam, M. L. Lai, P. Docampo, R. Higler, F. Deschler, M. Price, A. Sadhanala, L. M. Pazos, D. Credgington, F. Hanusch, T. Bein, H. J. Snaith and R. H. Friend, *Nat. Nanotechnol.*, 2014, **9**, 687–692.
13 G. L. Protesescu, S. Yakunin, M. I. Bodnarchuk, F. Krieg, R. Caputo, C. H. Hendon, R. X. Yang, A. Walsh and M. V. Kovalenko, *Nano Lett.*, 2015, **15**, 3692–3696.
14 C. K. Ng, C. Wang and J. J. Jasieniak, *Langmuir*, 2019, **35**, 11609–11628.
15 J. Shamsi, A. S. Urban, M. Imran, L. De Trizio and L. Manna, *Chem. Rev.*, 2019, **119**, 3296–3348.
16 G. Almeida, L. Goldoni, Q. Akkerman, Z. Dang, A. H. Khan, S. Marras, I. Moreels and L. Manna, *ACS Nano*, 2018, **12**, 1704–1711.
17 H. Pan, X. Li, X. Zhang, J. Liu, X. Chen, H. Zhang, A. Huang and Z. Xiao, *Langmuir*, 2020, **36**, 13663–13669.
18 R. Grisorio, D. Conelli, R. Giannelli, E. Fanizza, M. Striccoli, D. Altamura, C. Giannini, I. Allegretta, R. Terzano and G. P. Suranna, *Nanoscale*, 2020, **12**, 17053–17063.
19 S. Seth and A. Samanta, *Sci. Rep.*, 2016, **6**, 37693.
20 C. Lu, M. W. Wright, X. Ma, H. Li, D. S. Itanze, J. A. Carter, C. A. Hewitt, G. L. Donati, D. L. Carroll, P. M. Lundin and S. M. Geyer, *Chem. Mater.*, 2019, **31**, 62–67.
21 L. Hu, C. Wang, R. M. Kennedy, L. D. Marks and K. R. Inorg, *Chem.*, 2015, **54**, 740–745.
22 J. C. Sadighian, M. L. Crawford, T. W. Suder and C. Y. Wong, *J. Mater. Chem. C*, 2020, **8**, 7041–7050.
23 A. Chakrabarty, S. Satija, U. Gangwar and S. Sapra, *Chem. Mater.*, 2020, **32**, 721–733.
24 J. C. Sadighian, M. L. Crawford, T. W. Suder and C. Y. Wong, *J. Mater. Chem. C*, 2020, **8**, 7041–7050.
25 H. Lee, J. W. Jeong, M. G. So, G. Y. Jung and C.-L. Lee, *Adv. Mater.*, 2021, **33**, 2007855.
26 K. Hills-Kimball, H. Yang, T. Cai, J. Wang and O. Chen, *Adv. Sci.*, 2021, **8**, 2100214.
27 Y. Ding, Z. Zhang, S. Toso, I. Gushchina, V. Trepalin, K. Shi, J. W. Peng and M. Kuno, *J. Am. Chem. Soc.*, 2023, **145**, 6362–6370.
28 J. Qiu, W. Xue, W. Wang and Y. Li, *Dyes Pigm.*, 2022, **198**, 109806.
29 J. Shamsi, A. S. Urban, M. Imran, L. De Trizio and L. Manna, *Chem. Rev.*, 2019, **119**, 3296–3348.
30 M. Imran, P. Ijaz, D. Baranov, L. Goldoni, U. Petralanda, Q. Akkerman, A. L. Abdelhady, M. Prato, P. Bianchini, I. Infante and L. Manna, *Nano Lett.*, 2018, **18**, 7822–7831.
31 S. Xing, Y. Lian, R. Lai, X. Cao, M. Yu, G. Zhang, B. Zhao and D. Di, *J. Phys. Chem. Lett.*, 2022, **13**, 704–710.
32 C. R. Mayer, H. Levy-Falk, M. Rémond, G. Trippé-Allard, F. Fossard, M. Vallet, M. Lepeltier, N. Guiblin, J.-S. Lauret, D. Garrot and E. Deleporte, *Chem. Commun.*, 2022, **58**, 5960–5963.
33 J. H. Warby, B. Wenger, A. J. Ramadan, R. D. J. Oliver, H. C. Sansom, A. R. Marshall and H. J. Snaith, *ACS Nano*, 2020, **14**, 8855–8865.
34 Y. Yan, S. Yu, A. Honarfar, T. Pullerits, K. Zheng and Z. Liang, *Adv. Sci.*, 2019, **6**, 1900548.
35 Y. F. Ng, B. Febriansyah, N. F. Jamaludin, D. Giovanni, N. Yantara, X. Y. Chin, Y. B. Tay, T. C. Sum, S. Mhaisalkar and N. Mathews, *Chem. Mater.*, 2020, **32**, 8097–8105.
36 (*a*) P. Pang, G. Jin, C. Liang, B. Wang, W. Xiang, D. Zhang, J. Xu, W. Hong, Z. Xiao, L. Wang, G. Xing, J. Chen and D. Ma, *ACS Nano*, 2020, **14**, 11420–11430; (*b*) G. Delport, G. Chehade, F. Lédée, H. Diab, C. Milesi-Brault, G. Trippé-Allard, J. Even, J. S. Lauret, E. Deleporte and D. Garrot, *J. Phys. Chem. Letter*, 2019, **10**, 5153–5159.
37 A. De, N. Mondal and A. Samanta, *J. Phys. Chem. C*, 2018, **122**, 13617–13623.
38 Y. Gao, Z. Wei, S.-N. Hsu, B. W. Boudouris and L. Dou, *Mater. Chem. Front.*, 2020, **4**, 3400–3418.
39 M. C. Gélvez-Rueda, W. T. M. Van Gompel, R. Herckens, L. Lutsen, D. Vanderzande and F. C. Grozema, *J. Phys. Chem. Lett.*, 2020, **11**, 824–830.
40 S. Toso, D. Baranov, C. Giannini, S. Marras and L. Manna, *ACS Mater. Lett.*, 2019, **1**, 272–276.
41 J. Liu, X. Zheng, O. F. Mohammed and O. M. Bakr, *Acc. Chem. Res.*, 2022, **55**, 262–274.
42 F. Bertolotti, A. Vivani, F. Ferri, P. Anzini, A. Cervellino, M. I. Bodnarchuk, G. Nedelcu, C. Bernasconi, M. V. Kovalenko, N. Masciocchi and A. Guagliardi, *Chem. Mater.*, 2022, **34**(2), 594–608.
43 C. K. Ng, W. Yin, H. Li and J. J. Jasieniak, *Nanoscale*, 2020, **12**, 4859–4867.
44 J. Song, J. Li, L. Xu, J. Li, F. Zhang, B. Han, Q. Shan and H. Zeng, *Adv. Mater.*, 2018, **30**, 1800764.
45 S. Akhil, V. G. Vasavi Dutt, R. Singh and N. Mishra, *J. Phys. Chem. C*, 2022, **126**, 10742–10751.
46 Y. Wang, F. Yang, X. Li, F. Ru, P. Liu, L. Wang, W. Ji, J. Xia and X. Meng, *Adv. Funct. Mater.*, 2019, **29**, 1904913.
47 J.-R. Wen, F. A. R. Ortiz, A. Champ and M. T. Sheldon, *ACS Nano*, 2022, **16**, 8318–8328.
48 T. Wu, Y. Wang, Z. Dai, D. Cui, T. Wang, X. Meng, E. Bi, X. Yang and L. Han, *Adv. Mater.*, 2019, **31**, 1900605.
49 Y. Wei, Z. Cheng and J. Lin, *Chem. Soc. Rev.*, 2019, **48**, 310.
50 J. Zhu, Q. Di, X. Zhao, X. Wu, X. Fan, Q. Li, W. Song and Z. Quan, *Inorg. Chem.*, 2018, **57**, 6206–6209.
51 Q. Sun, C. Ni, Y. Yu, S. Attique, S. Wei, Z. Ci, J. Wang and S. Yang, *J. Mater. Chem. C*, 2018, **6**, 12484–12492.

52 L. Yang, T. Wang, Q. Min, B. Liu, Z. Liu, X. Fan, J. Qiu, X. Xu, J. Yu and X. Yu, *ACS Omega*, 2019, **4**, 6084–6091.
53 J. Yin, H. Yang, K. Song, A. M. El-Zohry, Y. Han, O. M. Bakr, J.-L. Brédas and O. F. Mohammed, *J. Phys. Chem. Lett.*, 2018, **9**, 5490–5495.
54 B. Hudait, S. K. Dutta, S. Bera and N. Pradhan, *Nano Lett.*, 2021, **21**, 5277–5284.
55 J. Cui, F. Xu, Q. Dong, J. Jia, L. Liu, S. Liu, F. Yang and X. Ye, *Mater. Res. Bull.*, 2020, **124**, 110731.
56 S. K. Dutta, S. Bera, R. K. Behera, B. Hudait and N. Pradhan, *ACS Nano*, 2021, **15**, 16183–16193.
57 M. Li, X. Zhang, T. Dong, P. Wang, K. Matras-Postolek and P. Yang, *J. Phys. Chem. C*, 2018, **122**, 28968–28976.
58 J. Liu, K. Song, X. Zheng, J. Yin, K. X. Yao, C. Chen, H. Yang, M. N. Hedhili, W. Zhang, P. Han, O. F. Mohammed, Y. Han and O. M. Bakr, *J. Phys. Chem. Lett.*, 2021, **12**, 10402–10409.
59 S. Wei, Y. Yang, X. Kang, L. Wang, L. Huang and D. Pan, *Inorg. Chem.*, 2017, **56**, 2596–2601.
60 L. Ruan, W. Shen, A. Wang, A. Xiang and Z. Deng, *J. Phys. Chem. Lett.*, 2017, **8**, 3853–3860.
61 A. Dutta, R. K. Behera, S. K. Dutta, S. Das Adhikari and N. Pradhan, *J. Phys. Chem. Lett.*, 2018, **9**, 6599–6604.
62 X. Tang, S. Han, Z. Zu, W. Hu, D. Zhou, J. Du, Z. Hu, S. Li and Z. Zang, *Front. Phys.*, 2018, **5**(69), 1–7.
63 L. Ruan, J. Lin, W. Shen and Z. Deng, *Nanoscale*, 2018, **10**, 7658–7665.
64 K.-H. Wang, L. Wu, L. Li, H.-B. Yao, H.-S. Qian and S.-H. Yu, *Angew. Chem., Int. Ed.*, 2016, **55**, 8328–8332.
65 J. Zhao, S. Cao, Z. Li and N. Ma, *Chem. Mater.*, 2018, **30**, 6737–6743.
66 Y.-L. Hu, Q.-L. Wen, Z.-F. Pu, A.-Y. Liu, J. Wang, J. Ling, X.-G. Xie and Q.-E. Cao, *RSC Adv.*, 2020, **10**, 34215.
67 T. Udayabhaskararao, M. Kazes, L. Houben, H. Lin and D. Oron, *Chem. Mater.*, 2017, **29**, 1302–1308.
68 Z. Dang, J. Shamsi, F. Palazon, M. Imran, Q. A. Akkerman, S. Park, G. Bertoni, M. Prato, R. Brescia and L. Manna, *ACS Nano*, 2017, **11**, 2124–2132.
69 H. Lee, J. W. Jeong, M. G. So, G. Y. Jung and C.-L. Lee, *Adv. Mater.*, 2021, **33**, 2007855.
70 X.-K. Liu, W. Xu, S. Bai, Y. Jin, J. Wang, R. H. Friend and F. Gao, *Nat. Mater.*, 2021, **20**, 10.
71 R. J. Hill, *Acta Crystallogr.*, 1985, **41**, 1281–1284.
72 A. Kostopoulou, M. Sygletou, K. Brintakis, A. Lappas and E. Stratakis, *Nanoscale*, 2017, **9**, 18202–18207.
73 J. Xing, Y. Zhao, M. Askerka, L. N. Quan, X. Gong, W. Zhao, J. Zhao, H. Tan, G. Long, L. Gao, Z. Yang, O. Voznyy, J. Tang, Z.-H. Lu, Q. Xiong and E. H. Sargent, *Nat. Commun.*, 2018, **9**, 3541.
74 Y. Li, J. V. Milić, A. Ummadisingu, J.-Y. Seo, J.-H. Im, H.-S. Kim, Y. Liu, M. I. Dar, S. M. Zakeeruddin, P. Wang, A. Hagfeldt and M. Grätzel, *Nano Lett.*, 2019, **19**(1), 150–157.
75 L. Mao, C. C. Stoumpos and M. G. Kanatzidis, *J. Am. Chem. Soc.*, 2019, **141**, 1171–1190.
76 Q. Jing, Y. Xu, Y. Su, X. Xing and Z. Lu, *Nanoscale*, 2019, **11**, 1784–1789.
77 J. H. Park, A.-Y. Lee, J. C. Yu, Y. S. Nam, Y. Choi, J. Park and M. H. Song, *ACS Appl. Mater. Interfaces*, 2019, **11**, 8428–8435.
78 X. Li, J. M. Hoffman and M. G. Kanatzidis, *Chem. Rev.*, 2021, **121**(4), 2230–2291.
79 J. Y. Lee, S. Y. Kim and H. J. Yoon, *Adv. Opt. Mater.*, 2022, **10**, 2101361.
80 H. Song, J. Yang, W. H. Jeong, J. Lee, T. H. Lee, J. W. Yoon, H. Lee, A. J. Ramadan, R. D. J. Oliver, S. C. Cho, S. G. Lim, J. W. Jang, Z. Yu, J. T. Oh, E. D. Jung, M. H. Song, S. H. Park, J. R. Durrant, H. J. Snaith, S. U. Lee, B. R. Lee and H. Choi, *Adv. Mater.*, 2023, **35**, 2209486.
81 M. D. Smith, B. A. Connor and H. I. Karunadasa, *Chem. Rev.*, 2019, **119**, 3104–3139.
82 C. Lee, Y. Shin, A. Villanueva-Antolí, S. Das Adhikari, J. Rodriguez-Pereira, J. M. Macak, C. A. Mesa, S. Giménez, S. J. Yoon, A. F. Gualdrón-Reyes and I. Mora-Seró, *Chem. Mater.*, 2021, **33**(22), 8745–8757.